JOM, Vol. 74, No. 12, 2022
https://doi.org/10.1007/s11837-022-05540-5

Performance and Durability of Reversible Solid Oxide Cells with Nano-electrocatalysts Infiltrated Electrodes

MIAO YU,[1] XIAOFENG TONG,[2,3] BHASKAR REDDY SUDIREDDY,[1] and MING CHEN [1,4]

1.—Department of Energy Conversion and Storage, Technical University of Denmark, 2800 Kongens Lyngby, Denmark. 2.—Institute of Energy Power Innovation, North China Electric Power University, Beijing 102206, China. 3.—e-mail: xiaofeng.tong@ncepu.edu.cn. 4.—e-mail: minc@dtu.dk

This work focuses on improving the durability of Ni/yttria-stabilized zirconia (YSZ) fuel electrode-supported solid oxide cells under the reversible operation mode by infiltrating nano-sized electrocatalysts into both electrodes. The resulting cell consists of a CGO (Gd-doped CeO_2) scaffold-based oxygen electrode that is infiltrated with LSC ($La_{0.6}Sr_{0.4}CoO_{3-\delta}$) and CGPO (Gd, Pr-co-doped CeO_2) nanocomposite infiltrates and a Ni/YSZ fuel electrode modified with nano-CGO infiltrates. Constant-current tests at + 0.5 A/cm^2 and − 0.5 A/cm^2 are carried out, followed by cycling between fuel-cell and electrolysis modes at ± 0.5 A/cm^2 and ± 1.25 A/cm^2. Under the reversible operation at ± 0.5 A/cm^2, the cell showed lower degradation rates than under the single mode operation, with cell voltage degradation of 1.23%/kh in fuel cell mode and 0.53%/kh in electrolysis mode. During the cycling operation at ± 1.25 A/cm^2, the overall degradation rate under the electrolysis mode was only 0.46%/kh. Compared to the previously tested cells with only LSC infiltrated oxygen electrodes, the cell tested in this work shows better durability with degradation rates of less than half of the previous tests. The results in this work demonstrate that infiltrating nano-electrocatalysts into both electrodes is an effective solution to boost cell performance and durability under reversible operation.

INTRODUCTION

Strong demand for generating electricity from clean and renewable energy has appeared worldwide. However, renewables like wind and solar power are intermittent, and sometimes they are not available when needed. Thus, to balance the use and demand requests, efficient and inexpensive energy conversion and storage systems are required to store the intermittent renewable energies and further convert them into other energy forms. Electrolysis technologies can convert renewable electricity into hydrogen from water or carbon monoxide from carbon dioxide. Furthermore, synthetic gases like methane (CH_4), methanol (CH_3OH), and other CO_2-neutral fuels are likely to be produced through syngas (CO + H_2).[1,2] A reversible solid oxide cell (rSOC) can be operated as either a solid oxide fuel cell (SOFC) or a solid oxide electrolysis cell (SOEC) depending on its operating conditions. Under SOEC mode, electrical energy is converted into chemical energy and stored as H_2 or syngas through steam or co-electrolysis of steam and CO_2. Syngas can be further converted into liquid hydrocarbon fuels through catalytic chemical processes such as Fischer–Tropsch synthesis.[2–5] Under SOFC mode, the produced H_2 or syngas can be used as fuel to generate electricity and heat. By combining the SOFC and SOEC in one device, an rSOC can convert the surplus off-peak electricity from renewables into H_2 or syngas through electrolysis and use the produced gas to generate cheap electricity during the peak hours. Jensen et al.[6] described a novel storage method consisting of an

(Received July 28, 2022; accepted September 20, 2022; published online October 18, 2022)

rSOC combined with sub-surface CO_2 and CH_4 storage. The round-trip efficiency exceeded 70%, and the storage cost was only 0.03$/kWh according to their estimation.

Good performance and long-term durability are required for the commercialization of rSOC technology. In the past decade, different electrode materials, microstructure of the electrodes, and operating conditions have been studied.[10–13] Lang et al.[11] reported the long-term durability performance of an SOC stack consisting of 30 electrolyte-supported cells (ESCs) supplied by Sunfire. The stack was operated for 3370 h in constant SOEC mode at 820°C followed by 2500 h in reversible SOFC/SOEC mode with the steam utilization of 70%. A higher degradation rate of 1.2%/kh under SOEC mode was found during the reversible operation, higher than that under constant SOEC operation (0.5%/kh) at −520 mA/cm^2. Under SOFC mode during the reversible operation, the degradation was higher, i.e., 3.1%/kh at 750°C. Optimizing the operating conditions for reversible cycling was suggested to decrease the stack degradation. In the EU-funded project REFLEX (Analysis of the European energy system under the aspects of flexibility and technological progress), the effects of current density, steam content, and the utilization degree were studied for the load cycling operation on the Ni/YSZ-based cells.[12,13] Differently, they found that at a high current density (− 1.2 A/cm^2), the degradation rates under the SOEC mode significantly decreased during the load cycling operation compared to the constant SOEC operation. From the post-mortem investigation, microstructural changes such as detachment of Ni particles, Ni migration, and silica-rich impurities were observed in the fuel electrode after the load-cycling operation.

The EU-funded project BALANCE (Increasing penetration of renewable power, alternative fuels and grid flexibility by cross-vector electrochemical processes) aimed to accelerate the development of European rSOC technology by identifying and analyzing the national activities and coordinating research efforts into all aspects of rSOC. In the previous work, Sun et al.[10] studied the effect of different cell types, operating temperatures, and applied current density on the rSOC performance. A comparable degradation rate of < 7%/kh was achieved for SOEC cells with either LSC/CGO composite oxygen electrode operated at ± 0.5 A/cm^2 or LSC infiltrated oxygen electrode at ± 1.25 A/cm^2. They also found that high degradation mainly originated from the Ni/YSZ electrode. On the other hand, Tong and Ovtar et al.[14,15] successfully improved the cell performance and durability by infiltrating electrocatalysts into the porous electrodes. Inspired by the previous studies, the present work focuses on the electrochemical performance of a nano-engineered rSOC, with both electrodes infiltrated with nano-electrocatalysts. The performance and durability of the cell during the galvanostatic SOFC/SOEC operations and the reversible operation at both ± 0.5 A/cm^2 and ± 1.25 A/cm^2 are studied.

EXPERIMENTAL

Cell Specifications and Infiltration Procedure

The cell tested in this work was a Ni/YSZ (yttria-stabilized zirconia) fuel electrode supported cell (size of 5.3 × 5.3 cm^2 with an active area of 16 cm^2) produced at DTU. The cell consists of a Ni/3YSZ (zirconia stabilized with 3 mol% yttria) fuel electrode support layer (300 μm in thickness), a Ni/8YSZ (zirconia stabilized with 8 mol% yttria) active layer (10 μm), a dense 8YSZ electrolyte (10 μm), a CGO barrier layer (6 μm) between electrolyte and oxygen electrode, and a porous CGO backbone. The support layer, fuel active electrode, electrolyte, barrier layer, and porous backbone layer were fabricated by multilayer tape casting process (MTC) followed by sintering. The details of cell manufacturing were illustrated elsewhere.[10] After reducing the fuel electrode from NiO/YSZ to Ni/YSZ, the CGO scaffold was infiltrated with CGPO (Gd, Pr-co-doped CeO_2) and LSC ($La_{0.6}Sr_{0.4}CoO_{3-\delta}$) aqueous nitrate solutions, and the Ni/YSZ fuel electrode was infiltrated with CGO ($Ce_{0.8}Gd_{0.2}O_{2-\delta}$) nitrate solution. The nitrate solutions contain the stoichiometric amount of the respective metal nitrates and surfactants to improve the wetting of the surface. After each infiltration, the cell was calcined at 300°C. The infiltration cycles were repeated until the required amounts of electrocatalyst loadings were achieved. The infiltration method was described in detail previously[14] and is illustrated in Fig. 1. After infiltration, a 30-μm-thick LSC contact layer was screen-printed on top of the oxygen electrode with an active area of 4 × 4 cm^2.

Testing Scheme

The single cell testing was conducted at DTU's testing lab. The cell was mounted in an alumina cell test house. Ni and Au meshes were used as current collectors for the fuel electrode and oxygen electrode, respectively. A gold frame (0.8 mm thickness) was applied to seal the fuel electrode side. The set-up for single-cell testing was illustrated elsewhere.[16] As startup, the cell was heated up to 800°C with a ramp of 1°C/min, with 50 L/h air to the oxygen electrode and safety H_2 (N_2/H_2 = 95/5) to the fuel electrode. The initial performance characterization was carried out at 800°C, with 24 L/h H_2 + 4% H_2O to the fuel electrode and 140 L/h air to the oxygen electrode. After that, the cell was brought to 700°C and the AC electrochemical impedance spectroscopy (EIS) measurements were performed by varying the gas atmosphere on both sides. The oxygen electrode was supplied with 50 L/h air or O_2, and the fuel electrode was supplied with 24 L/h H_2 with 4%, 20%, and 50% steam.

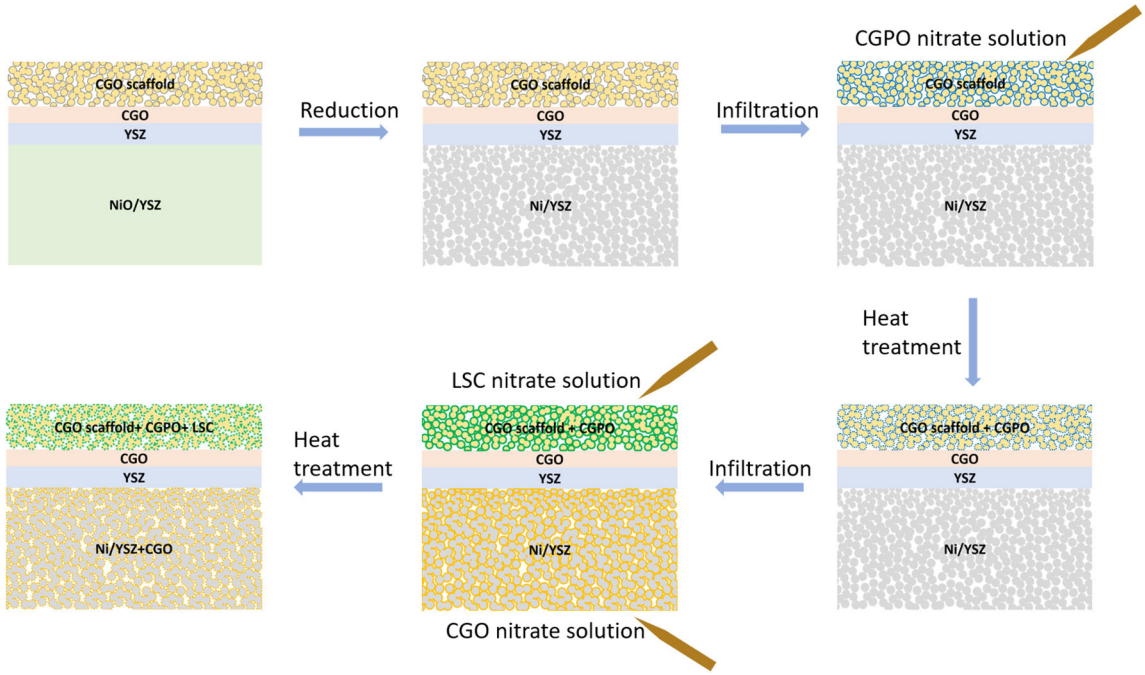

Fig. 1. Schematic illustration of the infiltration steps.

Table I. Operating time/cycles, gas composition to the fuel and oxygen electrodes, and applied current densities during each operating step

Test mode	Time / cycles	Gas composition to the fuel electrode	Gas composition to the oxygen electrode	Current density (A/cm^2)
Constant SOFC	120 h	12.8 L/h H_2/N_2 (H_2/N_2 = 50/50)	59.1 L/h air	0.5
Constant SOEC	120 h	8 L/h H_2/H_2O (H_2/H_2O = 20/80)	11 L/h air	−0.5
Reversible operation at low current density	3 h SOFC + 20 h SOEC + 1 h transition; 33 cycles in total	SOFC: 12.8 L/h H_2/N_2 (H_2/N_2 = 50/50); SOEC: 8 L/h H_2/H_2O (H_2/H_2O = 20/80)	SOFC: 59.1 L/h air; SOEC: 11 L/h air	± 0.5
Reversible operation at high current density	3 h SOFC + 20 h SOEC + 1 h transition; 34 cycles in total	SOFC: 32 L/h H_2/N_2 (H_2/N_2 = 50/50); SOEC: 20 L/h H_2/H_2O (H_2/H_2O = 20/80)	SOFC: 120 L/h air; SOEC: 24 L/h air	± 1.25

After the initial performance characterization, the durability test was carried out. The detailed test procedures are presented in Table I. A 120 h (5 days) of constant current SOFC pre-conditioning was carried out at the current density of 0.5 A/cm^2, with a total flow of 12.8 L/h H_2 + N_2 (H_2/N_2 = 50/50) supplied to the fuel electrode and 59.1 L/h air to the oxygen electrode. *i-V* and EIS characterizations were performed before and after the constant SOFC operation. After that, the SOEC pre-conditioning was performed at the current density of − 0.5 A/cm^2, with a total flow of 8 L/h H_2 + H_2O (H_2/H_2O = 20/80) supplied to the fuel electrode and 11 L/h air to the oxygen electrode. The reactant utilization was calculated as 52.3% under these conditions. Likewise, *i-V* and EIS characterizations were performed, followed by the reversible SOFC/SOEC operation. Each reversible cycle consisted of 3 h under SOFC mode and 20 h under SOEC mode plus 1 h for the transition periods, with the same gas compositions and current densities as in the previous constant condition tests. In each reversible operation cycle, the operation started with changing the gas composition to 12.8 L/h H_2/N_2 (H_2/N_2 = 50/50) to the fuel electrode compartment and 59.1 L/h air to the oxygen electrode compartment and then ramping up the current density to 0.5 A/cm^2 with a step of 0.125 A/cm^2. After operating for 3 h, the current density was ramped down to OCV, followed by changing the gas compositions and applying the

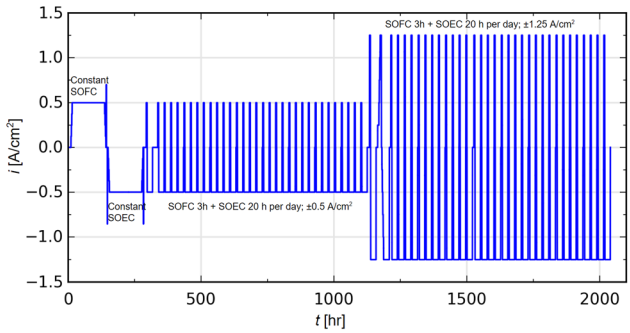

Fig. 2. Schematic of the current evolution as a function of time.

current density to −0.5 A/cm^2 for the 20 h SOEC operation. This reversible operation was run for 840 h with 33 cycles. EIS characterization was performed at a certain time during this reversible operation. After that, the current density was brought up to ± 1.25 A/cm^2. The operating procedure was the same as in the low current density reversible operation, with the gas compositions presented in Table I. After 34 cycles, the test was finished with a final fingerprint at 700°C. The schematic of the current evolution as a function of time is presented in Fig. 2.

Electrochemical Impedance Spectroscopy (EIS)

A Solartron 1255B frequency analyzer was used to measure the electrochemical impedance spectra (EIS) both at open-circuit voltage (OCV) conditions and under current during the constant SOFC/SOEC testing and the reversible operation. The spectra were recorded in a frequency range from 96,850 to 0.03 Hz with 12 points per decade. Ohmic resistance (R_s) and polarization resistance (R_p) were determined by measuring the high-frequency intercept and the difference between the high and low-frequency intercept of the real part of the impedance data. The distribution of relaxation times (DRT) method was used to identify and highlight frequency ranges for different electrode processes contributing to the total impedance response. To enable quantitative analysis, the EIS data were further fitted with an equivalent circuit model by the complex-non-linear-least-squares (CNLS) method. All the EIS data were analyzed by Python-based software RAVDAV.[17]

RESULTS

Initial Performance

Figure 3 presents the Nyquist plot and DRT plot during the initial fingerprint under OCV, with varying gas supplied to both electrodes. The DRT method has been used to clarify different types of processes that contribute to R_p. From Fig. 3, five peaks (P1-P5) were observable in the 1–20 kHz frequency range, each representing an

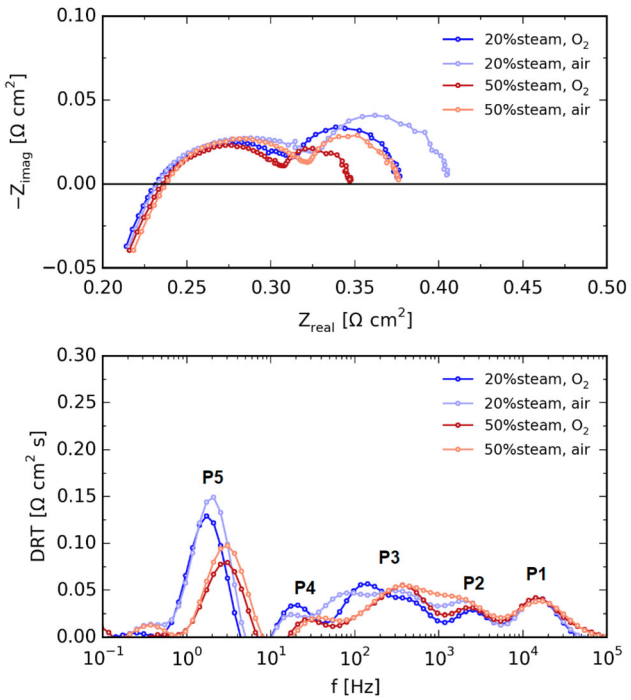

Fig. 3. EIS spectra recorded under OCV before the durability testing with varying gases supplied to both electrodes at 700°C and the corresponding DRT plot.

electrochemical, chemical or physical process occurring in the fuel or oxygen electrode. The area covered by each peak corresponds to the resistance of the corresponding process.[18,19]

As can be seen from the DRT plot, P1 remains almost identical to any gas changes, while P2-P5 change with the increased steam content in the fuel electrode from 20 to 50%. Besides, the process P3 seems to be sensitive to the gas composition of the oxygen electrode, i.e., pO_2 changes from switching air to pure O_2. The previous research[10,14,21–24] has summarized the process represented by each peak for the similar type of cells (Ni/YSZ-YSZ-CGO-LSC/CGO) investigated in this work. In Tong et al.'s work,[24] DRT plots at different temperatures (700–800°C) with varying gas supplied to the electrodes have been discussed. Five peaks were observed, with P1-P3 changing with operation temperatures whereas P4-P5 are temperature independent. Besides, similar to this work, they found that P2, P4, and P5 are related to the fuel electrode gas composition (H_2O content), and the change in P3 is related to the oxygen electrode gas composition (air or O_2). Therefore, the electrochemical processes regarding the peaks in different frequency ranges are concluded as the following: P1 is associated with the oxygen ions transport through the ionic conducting network in the electrodes and electrolyte. The major contribution is most likely from the YSZ network in the fuel electrode since the cell has a thick Ni/YSZ support layer, and the CGO scaffold in

the oxygen electrode is a highly ionic conducting material. P2 is associated with the electrochemical process that occurred in the triple-phase boundaries (TPBs) from the Ni/YSZ fuel electrode. P3 is related to the oxygen evolution reaction in the oxygen electrode. P4 and P5 represent the gas diffusion and gas conversion processes, respectively.

Constant-Current Operation

The evolution of cell voltage with time and the corresponding current density during the constant operation periods is presented in Fig. 4a. After the initial fingerprint, the tests were started with 120 h of constant galvanostatic SOFC testing at 0.5 A/cm^2 followed by 120 h of galvanostatic SOEC testing at − 0.5 A/cm^2. The cell showed stable performance during the constant SOFC and SOEC operation periods, with degradation rates of 15.78 mV/kh (1.96%/kh) and 24.65 mV/kh (2.14%/kh), respectively.

Figure 4b presents the *i-V* curves before and after the constant SOFC and SOEC operation periods. For both operation modes, the *i-V* curves before and after are almost identical, verifying the good durability of the cell during the constant operations. The OCV was measured as 1147.4 mV (with a cell temperature of 694.5°C) before the constant SOFC mode and 1142.5 mV (693.2°C) after the SOFC mode with 12.8 L/h H_2 + N_2 (H_2/N_2 = 50/50) to the fuel electrode and 59.1 L/h air to the oxygen electrode. Under the SOEC gas condition, the OCV was measured as 906.7 mV (692.2°C) and 906.9 mV (691.4°C) before and after the constant SOEC operation, respectively. The measured OCVs in SOEC mode are within 11 mV off the theoretical EMF (917.2 mV), indicating that the cell was sealed well.

To illustrate the R_s and R_p change during the constant-current tests, the EIS recorded during the durability testing periods is plotted in Fig. 5. The almost identical curves under the SOFC testing period confirm the observation from the stable cell voltage curves, while a slight increase of R_p is observed during the SOEC testing period. In the DRT plot, a minor increase of P3 and P4 during the 120 h operation was observable under both modes. In addition, an extra increase in P1 was observed for SOEC operation.

Reversible Operation

Figure 6a and b show the cell voltage change during the reversible operation at ± 0.5 A/cm^2 and ± 1.25 A/cm^2, respectively. In each daily cycle, the cell was operated for 3 h under SOFC mode and 20 h under SOEC mode plus 1 h for the transitions in-between. As can be seen, the cell voltage has minor changes at ± 0.5 A/cm^2 reversible operation. At ± 1.25 A/cm^2 reversible operation, cell voltage remains stable in the first 700 h and changed slightly in the last 200 h operation under both SOEC and SOFC modes. Figure 6c and d present the voltage change during the first and the last cycle for both reversible operations. At ± 0.5 A/cm^2 reversible operation, the evolutions of cell voltage

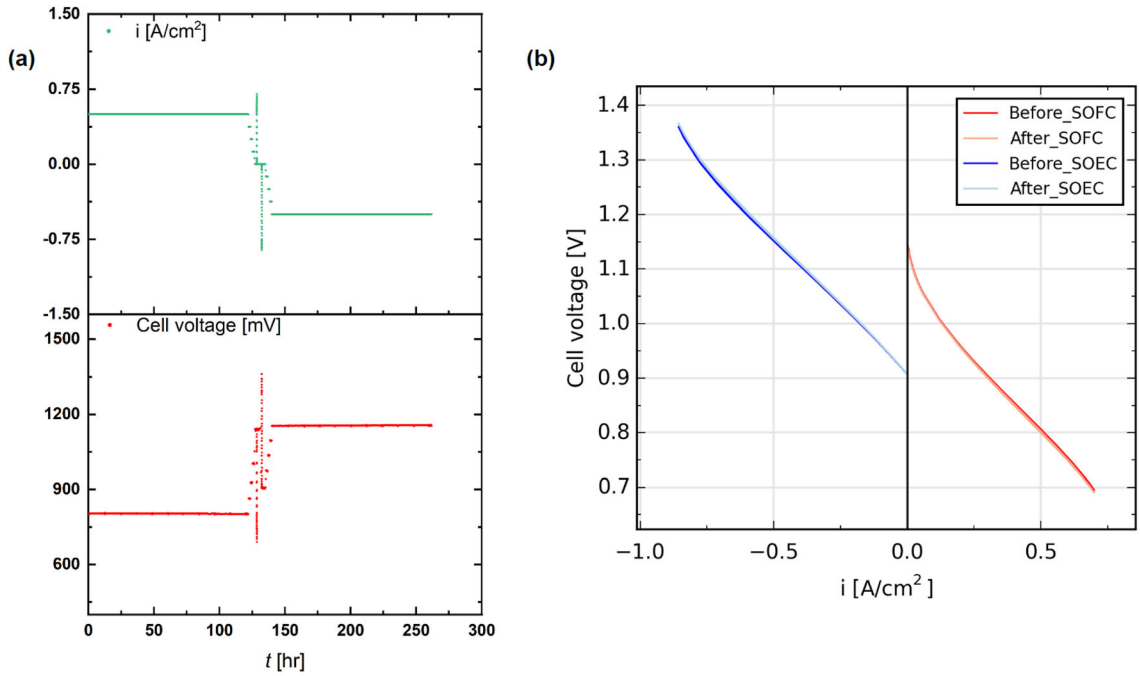

Fig. 4. (a) Evolution of cell voltage with time and the corresponding current density during the constant operation periods. (b) *i-V* curves before and after the constant SOFC and SOEC operation. Red curves: before and after the SOFC operation, with 12.8 L/h H_2 + N_2 (H_2/N_2 = 50/50) to the fuel electrode and 59.1 L/h air to the oxygen electrode. Blue curves: before and after the SOEC operation, with 8 L/h H_2 + H_2O (H_2/H_2O = 20/80) to the fuel electrode and 11 L/h air to the oxygen electrode (Color figure online).

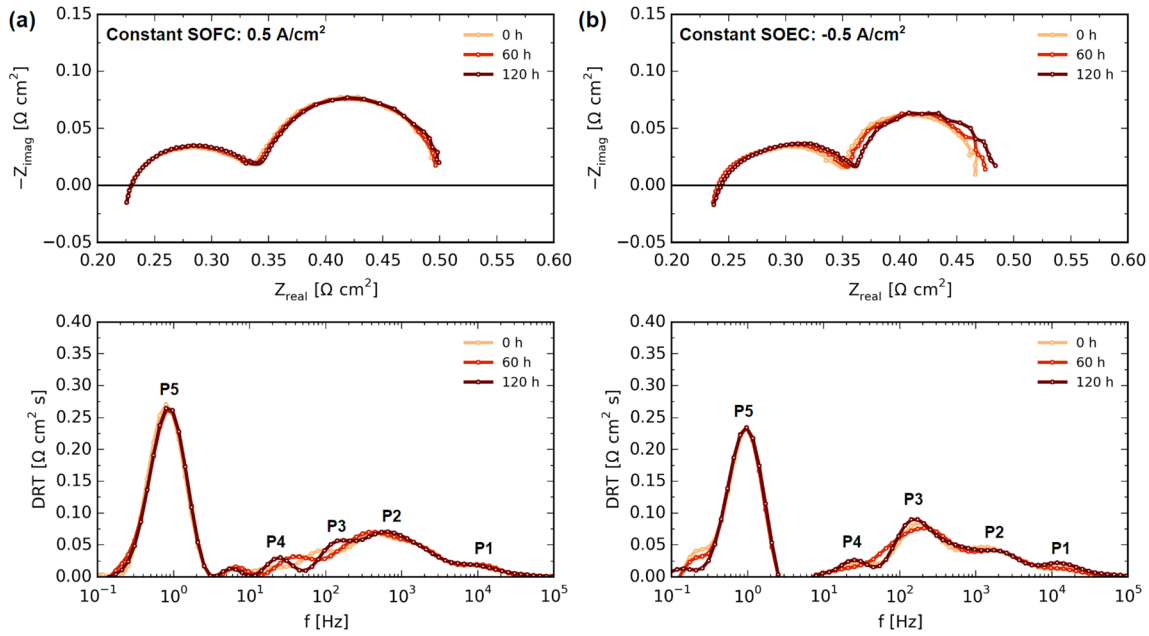

Fig. 5. Nyquist and DRT plots of the impedance spectra recorded during the 120 h galvanostatic operation periods at 700°C. (a) Constant SOFC operation at 0.5 A/cm^2, (b) constant SOEC operation at − 0.5 A/cm^2.

under both SOFC and SOEC modes are almost identical, confirming the stable performance of the cell during the reversible operation. Under the SOFC mode, the cell voltage degraded from 798 to 790 mV, and under the SOEC mode, it degraded only by 5 mV from 1157 to 1162 mV. At ± 1.25 A/cm^2 reversible operation, the cell voltages differentiate slightly between the first and the last cycle, especially under the SOFC mode. The cell voltage decreased by 20 mV from 561 to 541 mV under the SOFC mode, while under the SOEC mode, the voltage increased slightly by 6 mV from 1407 to 1413 mV.

Figure 7 presents the Nyquist plot and DRT plot during the reversible operation modes. The EIS data were recorded approximately every 100 h, under OCV after the SOEC operation within certain reversible cycles. The Nyquist plots show that the polarization resistance at high current density operation is markedly smaller than that at low current density operation, especially in the low-frequency arc. Moreover, a smaller polarization resistance attributed to the gas conversion process (P5) at high current density operation can be observed in the DRT plot. This observation is well in line with the previous study that the gas conversion process is related to the gas flow rate.[22] The gas conversion resistance shows a smaller value with a high flow rate supply under the ± 1.25 A/cm^2 reversible mode. Besides, P3 which corresponds to the electrochemical process at the oxygen electrode, seems to slightly increase when operated at high current density reversible mode than that at low current density. In comparison, P2, which is associated with the electrochemical process at the fuel electrode TPBs, has a similar increase at both current densities. This indicates that the Ni/YSZ fuel electrode infiltrated with CGO was less sensitive to the reversible operation current density than the CGPO and LSC co-infiltrated oxygen electrode.

DISCUSSION

Figure 8 shows the overview of the cell voltage during the entire operation. During ± 0.5 A/cm^2 reversible operation, the degradation rate under SOFC mode (1.23%/kh) is slightly lower than that under the constant SOFC operation (1.96%/kh). In comparison, the cell performance seems to be improved under the SOEC mode during the reversible operation, with a degradation rate of 0.53%/kh compared to that of 2.14%/kh under the galvanostatic SOEC operation. Compared to the constant galvanostatic operation at ± 0.5 A/cm^2, the cell durability was improved during the reversible operation at ± 0.5 A/cm^2 with lower cell voltage degradation rates. However, it should be noted that the constant operation periods were only 120 h each, and therefore the degradation rates in such a short time are not as representative as the reversible operations due to the possible initial degradation. Tong et al.[14] tested the same cell with LSC-CGPO infiltrated CGO backbone and CGO modified Ni/YSZ electrode under galvanostatic steam electrolysis at -1 A/cm^2. In the durability testing, the cell was tested for over 900 h at 750°C with 90/10 H_2O + H_2 supplied to the fuel electrode and pure O_2 to the oxygen electrode. As a result, stable durability was

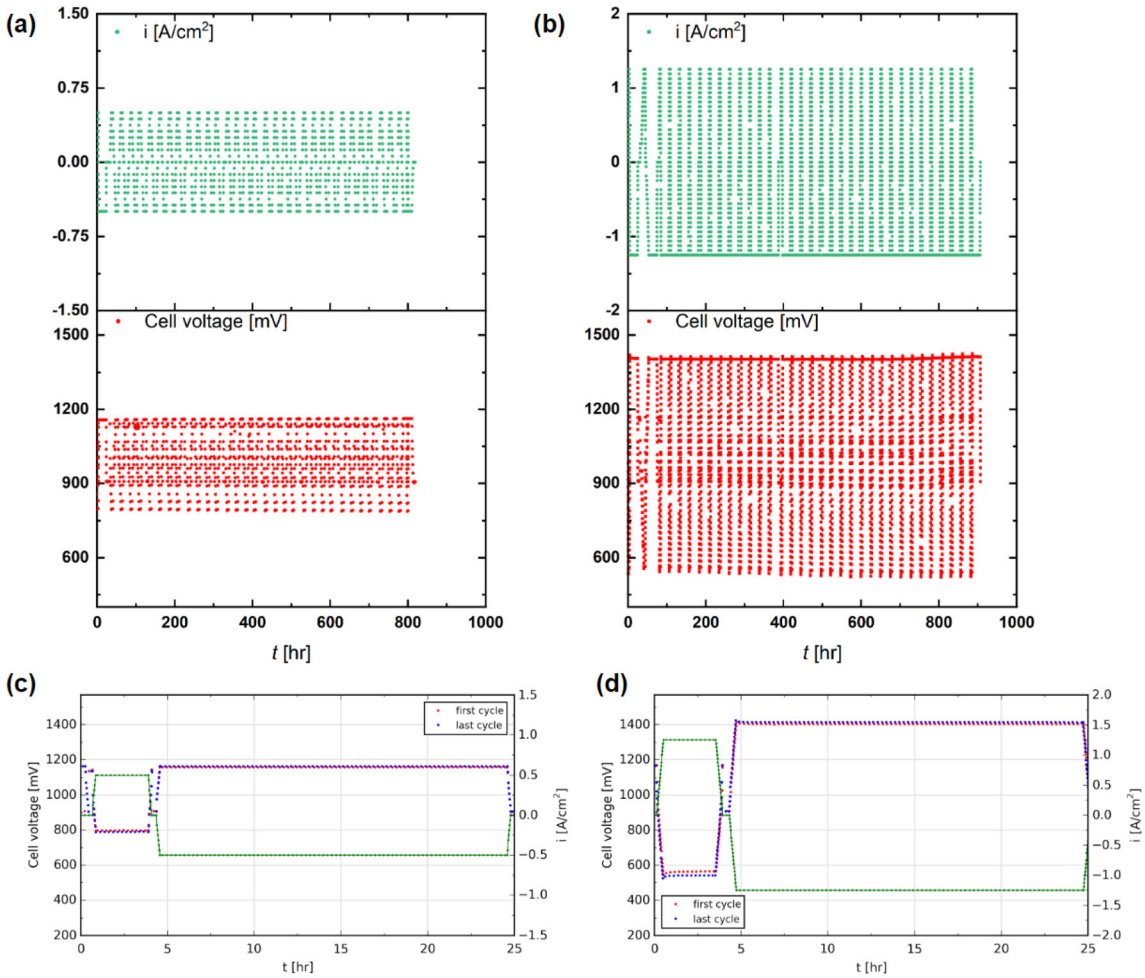

Fig. 6. Evolution of cell voltage with time and the corresponding current density during the reversible operation at (a) ± 0.5 A/cm^2, (b) ± 1.25 A/cm^2, (c) the first and the last cycles of the reversible operations at ± 0.5 A/cm^2, and (d) ± 1.25A/cm^2.

observed without initial degradation during the entire testing period with a degradation rate of 2.06%/kh, similar to what was observed in this work.

At ± 1.25 A/cm^2, the cell voltage seemed stable in the SOEC mode during the first 650 h of reversible operation. During the last 180 h (8 cycles), the cell voltage started to increase significantly with a degradation rate of 3.61%/kh. In SOFC mode, it was observed that the cell voltage dropped more than that at ± 0.5 A/cm^2. During the entire operating period at ± 1.25 A/cm^2, the degradation rate is 0.46%/kh under SOEC mode and 3.8%/kh under SOFC mode. The degradation rates calculated from the cell voltages for the different testing periods are listed in Table II.

The cell durability in this study was compared with that of the previous work by Sun et al.[10] In their experiment, two cells were tested under the same testing procedures at 700°C, i.e., 120 h constant operation under SOFC and SOEC modes followed by the reversible operation at ± 0.5 A/cm^2 or ± 1.25 A/cm^2, with 3 h under SOFC mode and 20 h under SOEC mode in each cycle. The cells tested in the previous work were in the same batch as the cell tested in this work, i.e., Ni/YSZ support layer, Ni/YSZ active electrode, YSZ electrolyte, CGO barrier layer, and porous CGO scaffold. Differently, the CGO scaffold was infiltrated with only LSC electrocatalyst, and no modification to Ni/YSZ was done in Sun et al.'s work. Data on the degradation rates based on cell voltage were extracted from Ref 10 and are presented in Table II. Under the constant operation mode, the cell in this work shows better performance under SOEC operation (2.14%/kh) than the cell infiltrated only with LSC (3.7%/kh). However, under galvanostatic SOFC operation, a lower degradation rate was found in the previously tested cell with a value of -1%/kh. During the reversible operation, lower degradation rates are seen for the cell tested in this work. Under the SOFC mode, the degradation rates in this work decreased by a factor of two compared to the previous tests at both ± 0.5 A/cm^2 and ± 1.25 A/cm^2. Under the SOEC mode, the degradation rate is found to be 0.53%/kh compared to that of 4% in the previous test at ± 0.5 A/cm^2. At ± 1.25 A/cm^2, the cell voltage seems to be stable until the last

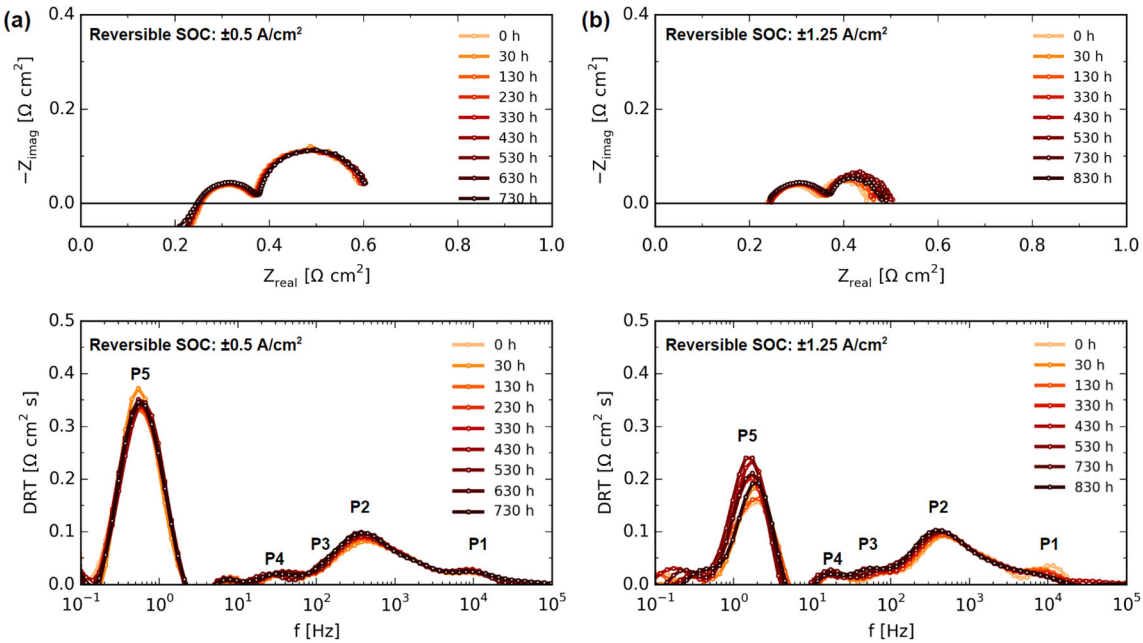

Fig. 7. Nyquist and DRT plots of the impedance spectra recorded during the reversible operation period at 700°C under OCV. (a) After the full cycle during the reversible operation at ± 0.5 A/cm^2 with 8 L/h H_2 + H_2O (H_2/H_2O = 20/80) supplied to the fuel electrode and 11 L/h air to the oxygen electrode, (b) during the reversible operation at ± 1.25 A/cm^2, with 20 L/h H_2 + H_2O (H_2/H_2O = 20/80) supplied to the fuel electrode and 24 L/h air to the oxygen electrode.

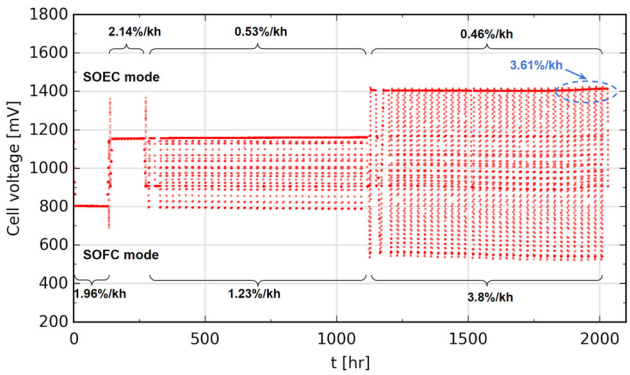

Fig. 8. Overview of the cell voltage change during the entire testing period and the corresponding degradation rates.

180 h (8 cycles), when it started to increase significantly with a degradation rate of 3.61%/kh. During the entire operating period at ± 1.25 A/cm^2, the degradation rate is found to be 0.46%/kh, significantly improved compared to that of 6.3%/kh in the previous test. The results show that infiltrating electrocatalysts into both the fuel and oxygen electrodes is a valid method to improve cell durability at reversible operations, especially under the SOEC mode and at high current densities. In Tong et al.'s work,[14] the role of infiltrated CGO in mitigating the degradation of the Ni/YSZ fuel electrode has been discussed. CGO nanoparticles which have mixed electronic and ionic conductivity play the role of facilitating the dissociation of H_2O as well as providing additional active sites for hydrogen evolution reaction on the Ni/YSZ. This extends the TPBs sites from Ni-YSZ-gas to Ni-CGO-gas as well as the two-phase boundary (2 PB) of CGO-gas (i.e., the surface of the CGO particles that are located on Ni grains). In this work, we also speculate that the CGO nanoparticles provide extra active sites on the Ni/YSZ electrode, thus improving cell durability for both constant and reversible operations. Further SEM analysis will be performed in our future work to validate the above speculations.

Hauch et al.[12] also found that load cycling operation leads to a decreased degradation rate. In their study, the cell was produced by Elcogen with an LSC oxygen electrode, CGO barrier layer, YSZ electrolyte, and Ni/YSZ fuel electrode. It was noticed that the degradation rates were significantly reduced at high current density load cycling operation (0.6 A/cm^2, −1.2 A/cm^2), especially under SOEC mode. The degradation rates under the SOEC mode were found to be < 3%/kh compared to that of 66–68%/kh under the 250 h constant SOEC operation. In another study,[20] reverse current treatment (RCT) was operated to reactivate the degraded Ni/YSZ fuel electrode. After the degradation under the CO_2 electrolysis with impurities or harsh steam electrolysis, the cells were treated with RCT, with cycles of 10 min in FC mode and 10–50 s in EC mode at various current densities (± 0.5—± 3 A/cm^2). The cells were degraded before the RCT treatment with increased resistance. However, R(Ni/YSZ TPB) decreased significantly after the RCT, indicating an increased TPB length in the fuel electrode active area. From their post-mortem SEM

Table II. Cell voltage degradation rates in different operation modes for the cell tested in this work and the cell tested in the previous work by Sun et al

Degradation rate, %/kh	Constant operation		Reversible operation ± 0.5 A/cm^2		Reversible operation ± 1.25 A/cm^2	
	SOFC	SOEC	SOFC	SOEC	SOFC	SOEC
This work	1.96 (15.78 mV/kh)	2.14 (24.65 mV/kh)	1.23 (9.80 mV/kh)	0.53 (6.08 mV/kh)	3.80 (21.28 mV/kh)	0.46 (6.44 mV/kh)
Sun et al	− 1	3.7	2.5	4	6.7	6.3

Data of the cell from the previous work were extracted from Ref. 10.

images, it was observable that additional Ni nanoparticles were formed in the weakened interface or detachment between the Ni particles and YSZ backbone, thereby adding the electrochemical active sites in the active fuel electrode structures via subsequent RCT. Graves et al.[26] also observed that the reversible operation of the Ni/YSZ supported SOC had negligible degradation compared to SOEC operation. They employed LSM/YSZ as the oxygen electrode. From the SEM images, they found that the main degradation of their SOEC cell operated at −1 A/cm^2 was the microstructure deterioration that occurred near the oxygen electrode/electrolyte interface, while the reversible cycling operation might slow down the O_2 bubble formation near the interface where high internal O_2 pressure builds up during high current density electrolysis operation. The oxygen bubble formation can be resolved by employing the LSCF/CGO oxygen electrode, which has much faster oxygen evolution reaction (ORR) kinetics than LSM/YSZ. The degradation of Ni/YSZ then becomes the bottleneck for long-term operation of SOEC cells with LSCF/CGO oxygen electrode, though with a degradation rate smaller than that with LSM/YSZ. Trini et al.[27] used focused ion beam (FIB)-SEM characterization and 3D reconstruction to study the degradation mechanism of the cell under SOEC and SOFC modes. They found that the cell under SOEC operation had much higher degradation compared to that under SOFC operation with the same durability testing conditions, where 24 L/h H_2 + H_2O (H_2/H_2O = 50/50) was supplied to the fuel electrode and 50 L/h O_2 to the LSCF/CGO oxygen electrode at 800°C and ± 1 A/cm^2. They observed from the 3D reconstruction that Ni depletion or Ni migrating away from the electrode/electrolyte interface is the main cause for SOEC degradation. Such Ni depletion or redistribution was not observed in the SOFC operation. Chen et al.[28] reported post-mortem analysis of the cells (Ni/YSZ-YSZ-LSM/YSZ) tested under steam and co-electrolysis conditions at 800–850°C and various current densities (0.5–1.5 A/cm^2). In the SEM images, the formation of ZrO_2 nanoparticles on Ni grains in the active fuel electrode region close to the fuel electrode/electrolyte interface was observed in the cells tested at

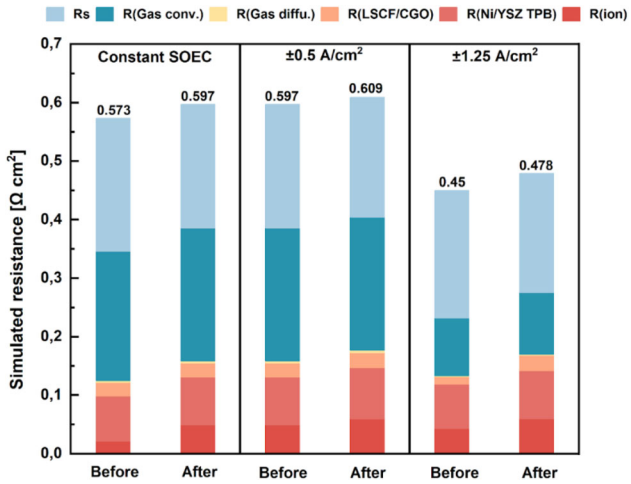

Fig. 9. Summary of the simulated values of Rs and resistances originated from different electrochemical processes under OCV at 700°C. Before and after the constant SOEC operation and ± 0.5 A/cm^2 reversible operation, 8 L/h H_2 + H_2O (H_2/H_2O = 20/80) was supplied to the fuel electrode and 11 L/h air was supplied to the oxygen electrode. Before and after the ± 1.25 A/cm^2 reversible operation, 20 L/h H_2 + H_2O (H_2/H_2O = 20/80) was supplied to the fuel electrode and 24 L/h air was supplied to the oxygen electrode.

high current density (≥ -1 A/cm^2). This introduces the detachment of the Ni–Ni and Ni-YSZ and deteriorates the Ni percolation in the active electrode, eventually resulting in the Ni/YSZ fuel electrode degradation. In our study, based on the electrochemical analysis, we speculate that the reversible operation, e.g., switching from the SOEC to SOFC mode in one cycle, slows down the degradation processes in Ni/YSZ happening in constant SOEC operation. At low current density (± 0.5 A/cm^2), the reversible operation retarded the Ni migration under electrolysis mode, while at high current density (± 1.25 A/cm^2), both Ni migration and formation of ZrO_2 nanoparticles during electrolysis operation seem to be inhibited or retarded. The contribution of the LSC/CGO oxygen electrode to the overall cell resistance and degradation is rather small; thus, the effect of reversible operation on the oxygen electrode degradation is difficult to clarify in the current work. The remaining

Table III. Values of different resistances originated from different electrochemical processes simulated by the equivalent circuit model through the CNLS method

Testing conditions	Constant SOEC		± 0.5 A/cm^2		± 1.25 A/cm^2	
	Before	After	Before	After	Before	After
Rs, Ω cm^2	0.227	0.211	0.211	0.205	0.218	0.203
R(ion), Ω cm^2	0.021	0.049	0.049	0.059	0.043	0.059
R(Ni/YSZ), Ω cm^2	0.077	0.082	0.082	0.088	0.075	0.082
R(LSC/CGO), Ω cm^2	0.024	0.024	0.024	0.025	0.013	0.026
R(diffu.), Ω cm^2	0.003	0.004	0.004	0.004	0.002	0.002
R(conv.), Ω cm^2	0.211	0.227	0.227	0.227	0.099	0.106
ASR, Ω cm^2	0.573	0.597	0.597	0.609	0.45	0.478

degradation in reversible operation could be caused by the processes like Ni coarsening, which is not affected by the mode of operation. Further analysis will be conducted and will be reported in the future work.

To quantitatively deconvolute different contributions from different electrochemical processes, the complex-non-linear-squares (CNLS) fitting method was used to fit the equivalent circuit model to the EIS data. The model consists of four constant phase elements (RQ) and a Gerischer element (G), which correspond to the five processes from the DRT analysis as discussed previously. Figure 9 and Table III summarize the simulated values of R_s and resistances from various electrochemical processes of the following tests under OCV: before and after the SOEC constant operation, ± 0.5 A/cm^2 reversible operation, and ± 1.25 A/cm^2 reversible operation. EIS data recorded before and after constant SOFC operation were invalid because of the measurement error. The EIS spectra before and after the SOEC constant operation and ± 0.5 A/cm^2 reversible operation were measured under the same operation conditions, with 8 L/h H_2 + H_2O (H_2/H_2O = 20/80) supplied to the fuel electrode and 11 L/h air supplied to the oxygen electrode. The EIS spectra measured before and after ± 1.25 A/cm^2 reversible operation were with different gas compositions: 20 L/h H_2 + H_2O (H_2/H_2O = 20/80) to the fuel electrode and 24 L/h air to the oxygen electrode. Therefore, the values before/after constant SOEC and ± 0.5 A/cm^2 reversible operation cannot be compared directly with the ones before/after ± 1.25 A/cm^2 reversible operation. From the simulated values, it can be noticed that the area specific resistance (ASR) increased slightly after each operating period. Among the different contributions to ASR, only R_s decreased. For example, ASR increased from 0.573 Ω cm^2 before the constant SOEC operation to 0.609 Ω cm^2 after the ± 0.5 A/cm^2 operation while the value of R_s decreased from 0.227 to 0.205 Ω cm^2. During the ± 1.25 A/cm^2 operation, ASR increased from 0.45 to 0.478 Ω cm^2 with a decrease of R_s from 0.218 to 0.203 Ω cm^2. The decrease of R_s might be due to the improved contacting during the testing. In comparison, R(ion) originated from the oxygen ionic transport network increased from 0.021 to 0.059 Ω cm^2. From the previous research,[20] it was concluded that R(ion) is mainly from the Ni/YSZ electrode, which has a much thicker and poorer ionic conducting network than that of the oxygen electrode. Resistance corresponding to the Ni/YSZ TPB process also increased from 0.077 to 0.088 Ω cm^2 after constant SOEC and ± 0.5 A/cm^2 reversible operation, from 0.075 to 0.082 Ω cm^2 after ± 1.25 A/cm^2 reversible operation. In comparison, the resistance from the oxygen electrode barely changed during the entire testing, suggesting that CGPO and LSC infiltrated oxygen electrode has stable performance during the galvanostatic and reversible operation. It is also observable that the gas conversion and gas diffusion resistances were both decreased by half after increasing the gas flow from 8 L/h H_2 + H_2O to 20 L/h H_2 + H_2O. This proves that the gas conversion and gas diffusion resistances are related to the gas flow supplied to the porous-structured electrode.[25,29] When a higher gas flow is supplied to the porous structure, the volume of the stagnant layer over the electrode is decreased, thereby gas diffusion resistance is reduced.

CONCLUSION

In this work, a planar SOC infiltrated with nano-sized electrocatalysts on both fuel and oxygen electrodes was investigated at constant-current and reversible cycling operation over 2000 h at 700°C. The cell showed good initial performance and excellent durability during both types of operation. The degradation rates under both SOFC and SOEC modes during the reversible operation were found to be lower than those during constant current operation at ± 0.5 A/cm^2, suggesting that reversible operation can decrease its degradation compared to the galvanostatic operation. Especially under SOEC mode, the degradation under the reversible operation was 0.53%/kh, four times smaller than that under the galvanostatic operation at −0.5 A/cm^2 (2.14%/kh). The simulated results from the CNLS analysis demonstrate that the resistance mainly

from the Ni/YSZ electrode increased during the constant SOEC and ± 0.5 A/cm^2 operation, whereas other contributions have only minor changes. This leads to an increase in ASR from 0.573 to 0.609 Ω cm^2 considering the value of R_s was decreasing. During the ± 1.25 A/cm^2 operation, ASR increased from 0.45 to 0.478 Ω cm^2, where the increased resistance contributions originated from both electrodes.

Compared to the previously tested cells with only LSC-modified oxygen electrodes, the cell tested in this work showed better cell durability during the reversible operation. The degradation rates under SOFC mode were decreased by a factor of two during both ± 0.5 and 1.25 A/cm^2 reversible cycling. During the ± 1.25 A/cm^2 reversible operation under the SOEC mode, the cell voltage degradation rates decreased significantly by a factor of 13, with a value of 0.46%/kh compared to 6.3%/kh from the previous work.[10] Findings in this work demonstrate that infiltrating the electrocatalysts on both electrodes is an effective method of boosting the cell performance and durability under the reversible operation and show the high potential of the improved Ni/YSZ-based cell for use at high current density r-SOC applications.

ACKNOWLEDGEMENTS

This work is supported by the project "BALANCE-Increasing penetration of renewable power, alternative fuels and grid flexibility by cross-vector electrochemical processes" under the European Union's Horizon 2020 research and innovation program (grant agreement no. 731224). M. Yu further acknowledges the project "Next Generation Power2X for Renewable Energy Conversion and Storage (NEXP2X)" (IFD no. 0143-00009B) and DTU Energy for supporting her PhD project. X. Tong acknowledges the support from the National Natural Science Foundation of China (Grant No. 52102244).

CONFLICT OF INTEREST

The authors declare that they have no conflict of interest.

OPEN ACCESS

REFERENCES

1. M.B. Mogensen, M. Chen, H.L. Frandsen, C. Graves, J.B. Hansen, K.V. Hansen, A. Hauch, T. Jacobsen, S.H. Jensen, T.L. Skafte, and X. Sun, *Clean Energy* 3, 175. (2019).
2. S.Y. Gómez and D. Hotza, *Renew. Sustain. Energy Rev.* 61, 155. (2016).
3. D.J. Wilhelm, D.R. Simbeck, A.D. Karp, and R.L. Dickenson, *Fuel Process. Technol.* 71, 139. (2001).
4. S.H. Jensen, P.H. Larsen, and M. Mogensen, *Int. J. Hydrogen Energy* 32, 3253. (2007).
5. J.P. Stempien, M. Ni, Q. Sun, and S.H. Chan, *Energy* 81, 682. (2015).
6. S.H. Jensen, C. Graves, M. Mogensen, C. Wendel, R. Braun, G. Hughes, Z. Gao, and S.A. Barnett, *Energy Environ. Sci.* 8, 2471. (2015).
7. M.P. Carpanese, M. Panizza, M. Viviani, E. Mercadelli, A. Sanson, and A. Barbucci, *J. Appl. Electrochem.* 45, 657. (2015).
8. M. Shiraki, H. Yakabe, and H. Uchida, *ECS Trans.* 57, 3261. (2013).
9. G.B. Jung, L.H. Fang, C.Y. Lin, X.V. Nguyen, C.C. Yeh, C.Y. Lee, J.W. Yu, S.H. Chan, W.T. Lee, S.W. Chang, and I.C. Kao, *Int. J. Electrochem. Sci.* 10, 9089. (2015).
10. X. Sun, B.R. Sudireddy, X. Tong, M. Chen, K. Brodersen, and A. Hauch, *ECS Trans.* 91, 2631. (2019).
11. M. Lang, S. Raab, M.S. Lemcke, C. Bohn, and M. Pysik, *Fuel Cells* 20, 690. (2020).
12. A. Hauch, S. Pylypko, G. Cubizolles, and J. Mouginn, *ECS Trans.* 103, 437. (2021).
13. A. Hauch, A. Ploner, S. Pylypko, G. Cubizolles, and J. Mougin, *Fuel Cells* 21, 467. (2021).
14. X. Tong, S. Ovtar, K. Brodersen, P.V. Hendriksen, M. Chen, and A.C.S. Appl, *Mater. Interfaces* 11, 25996. (2019).
15. S. Ovtar, X. Tong, J.J. Bentzen, K.T. Thydén, S.B. Simonsen, and M. Chen, *Nanoscale* 11, 4394. (2019).
16. S.D. Ebbesen, C. Graves, A. Hauch, H. Jensen Soren, and M. Mogensen, *J. Electrochem. Soc.* 157, B1419. (2010).
17. C. Graves, RAVDAV Data Analysis Software. Version 0.97 (2012).
18. A. Leonide, V. Sonn, A. Weber, and E. Ivers-Tiffée, *J. Electrochem. Soc.* 155, B36. (2008).
19. V. Sonn, A. Leonide, and E. Ivers-Tiffée, *J. Electrochem. Soc.* 155, B675. (2008).
20. X. Tong, P.V. Hendriksen, A. Hauch, X. Sun, and M. Chen, *J. Electrochem. Soc.* 167, 024519. (2020).
21. A. Hauch, M. Marchese, A. Lanzini, and C. Graves, *J. Power Sources* 377, 110. (2018).
22. P. Hjalmarsson, X. Sun, Y.-L. Liu, and M. Chen, *J. Power Sources* 262, 316. (2014).
23. A. Hauch, K. Brodersen, M. Chen, and M.B. Mogensen, *Solid State Ionics* 293, 27. (2016).
24. X. Tong, S. Ovtar, K. Brodersen, P.V. Hendriksen, and M. Chen, *J. Power Sources* 451, 227742. (2020).
25. S. Primdahl and M. Mogensen, *J. Electrochem. Soc.* 145, 2431. (1998).
26. C. Graves, S.D. Ebbesen, S.H. Jensen, S.B. Simonsen, and M.B. Mogensen, *Nat. Mater.* 14, 239. (2014).
27. M. Trini, A. Hauch, S. De Angelis, X. Tong, P.V. Hendriksen, and M. Chen, *J. Power Sources* 450, 227599. (2020).
28. M. Chen, Y. Liu, J.J. Bentzen, W. Zhang, X. Sun, A. Hauch, Y. Tao, J.R. Bowen, and P.V. Hendriksen, *J. Electrochem. Soc.* 160, F883. (2013).
29. S. Primdahl and M. Mogensen, *J. Electrochem. Soc.* 146, 2827. (1999).